Single-Anchor Ultra-Wideband Localization System Using Wrapped PDoA

Feng Ge [ID], *Student Member, IEEE* and Yuan Shen [ID], *Senior Member, IEEE*

Abstract—The ultra-wideband (UWB) technology has been widely used in high-accuracy localization systems benefiting from its superior time-resolution and stability. In recent years, the single-anchor localization (SAL) scheme has attracted intense interests with its high accuracy, low system complexity, and low deployment costs compared to traditional UWB localization schemes. In this paper, we develop a SAL system which achieves 3D high-accuracy localization using time and wrapped phase measurements of UWB signals. We expand the array aperture to improve the localization accuracy and address the phase wrapping problem using information fusion. Statistical characterization of ambiguous position estimates is encapsulated by soft positional information (SPI), which is approximated by Gaussian mixture model (GMM) to accelerate the filtering process. The parameters of GMM are estimated by an efficient parallel algorithm and two filtering methods are proposed to track the agent in different scenarios using approximate SPI. Finally, we implement the system on a low-cost platform and experimental results show that the proposed SAL system can achieve decimeter-level 3D localization accuracy in outdoor and indoor environments.

Index Terms—3D single-anchor localization, UWB antenna array, phase ambiguity, soft positional information, information fusion

1 INTRODUCTION

PRECISE localization technology enables many modern applications including navigation, Internet of Things (IoT), and emergency rescue [1], [2], [3]. Furthermore, 3D localization capability satisfies the demands of smart healthcare, smart factories, and unmanned aerial vehicle localization [4], [5], [6]. Global navigation satellite system (GNSS) can provide meter-level position information in outdoor open environments. However, because it is difficult for weak satellite signals to penetrate through walls, localization results of GNSS are unreliable in urban canyons and unavailable in indoor environments. To satisfy the demands for high-accuracy and reliable positioning services, a wide variety of localization technologies have been explored [7], such as radio frequency (RF)-based methods and pedestrian dead reckoning (PDR)-based methods [8], [9], [10].

Among existing localization methods, RF-based methods are widely used including Bluetooth [11], Wi-Fi [12], and radio-frequency identification (RFID) [13]. However, it is difficult to achieve 3D localization and sub-meter localization accuracy using these RF signals. The received signal strength indicator (RSSI) of RF signals are usually transformed into RF fingerprints [12] or distance measurements [13] to locate agents, which are susceptible to complex environments and will introduce meter-level localization errors. In addition to RSSI-based methods, there are also angle-of-arrival (AoA)-based methods using Wi-Fi signals [14] and

Bluetooth signals [15], which can achieve sub-meter localization accuracy but have only meter-level coverage.

Ultra-wideband (UWB) signals are superior in terms of time resolution, anti-multipath and anti-interference performance, and power consumption, because the UWB system transmits ultra-short pulses over a large bandwidth (>500 MHz) using a very low duty cycle [16], [17]. Based on UWB signals, time-of-flight (ToF) localization scheme [18] requires agents to measure distance to at least four anchors for 3D localization, which reduces the capacity of localization system severely. By strict clock synchronization between anchors, time-difference-of-arrival (TDoA) localization scheme can obtain positions using one UWB frame, which can serve more agents and is more energy-efficient.

Both ToF and TDoA localization schemes require multiple anchors to achieve localization, which is vulnerable to complex environments and increases system complexity and deployment costs. The single-anchor localization (SAL) scheme becomes one of current research trends, which can localize agents with a single anchor using multipath component (MPC) measurements [19], [20] or an antenna array [21], [22], [23]. Each MPC is associated with a virtual anchor (VA) by mirroring the single anchor at the corresponding reflective surface and the agent's position can be determined using VA measurements. When the anchor is equipped with an antenna array, hybrid ToF/AoA localization scheme is commonly used.

The antenna array estimates AoA of signals based on phase-difference-of-arrival (PDoA) measurements between different antennas [24], which provides higher localization accuracy than TDoA. PDoA is naturally restricted within the interval $[-\pi, \pi]$, which limits the antenna spacing to less than half-wavelength. When working at centimeter band, mutual coupling between antennas disturbs received signals and degrades the AoA-finding performance severely [25]. Expanding antenna spacings to larger than half-wavelength

• *The authors are with the Department of Electronic Engineering, Beijing National Research Center for Information Science and Technology, Tsinghua University, Beijing 100084, China. E-mail: ge-f16@mails.tsinghua.edu.cn, shenyuan_ee@tsinghua.edu.cn.*

can not only reduce antenna coupling, but also augment array aperture and improve AoA estimation accuracy [26]. However, the actual PDoA of signals cannot be obtained directly due to the phase wrapping problem [27], which can be solved by auxiliary measurements [28], [29].

In this paper, we develop a 3D SAL system based on UWB signals. The anchor consists of multiple synchronized UWB transceivers forming arbitrary geometry, each of which can identify the first path and provide estimate of time-of-arrival (ToA) and carrier phase, i.e., phase-of-arrival (PoA) [24]. 3D target localization can be achieved using these time and phase measurements. Expanding antenna spacings can improve localization accuracy, but will cause the phase wrapping problem. We exploit the concept of soft information [30], which retains statistical characterization of measurements, and encapsulate ambiguous positioning results into soft positional information (SPI). Gaussian mixture model (GMM) is used to approximate the SPI extracted from raw measurements with phase ambiguities, parameters of which are estimated by a parallel SPI estimation algorithm efficiently. Optionally, TDoA measurements can be incorporated into SPI, which provide significant assistance to ambiguity resolution. Finally, the approximate SPI is used for information fusion. In summary, we have following contributions in this paper:

- We design a 3D SAL system based on UWB signals using hybrid ToF/PDoA localization scheme and derive the performance metric in terms of squared position error bound (SPEB). Antenna spacings are above half-wavelength to achieve 3D high-accuracy localization, and we address the phase wrapping problem by information fusion.
- We develop a parallel SPI estimation algorithm to extract 3D SPI from raw measurements with phase ambiguities efficiently, which is approximated by GMM.
- We propose a Gaussian sum Kalman filter (GSKF) to achieve 3D localization in open space and a multi-grain grid-based filter [10] to locate pedestrians in complex indoor environments fusing map information, which can track the location ambiguity in SPI.
- We implement the proposed system on a low-cost platform. Experimental results demonstrate the accuracy of the proposed SAL system and the effectiveness of disambiguation method.

The rest of this paper is organized as follows. We discuss related works in Section 2 and the system overview in Section 3. In Section 4, we present the signal model and the performance metric of our system, and describe the parallel SPI estimation algorithm. Two filtering algorithms are presented in Section 5 to track location ambiguities in different scenarios. Simulation and experimental results are shown in Sections 6 and 7 concludes this paper.

Notation. Throughout this paper, we denote variables, vectors, and matrices as italic x, bold italic $\boldsymbol{x}$, and capital bold italic X, respectively. The notation $\mathbf{1}_n$ denotes a column vectors with n ones, and I_n denotes an n-dimensional unit matrix; $\mathrm{diag}(\boldsymbol{x})$ constructs a diagonal matrix with elements in $\boldsymbol{x}$; $[\cdot]^{\mathrm{T}}$ denotes the transpose operator; $\mathrm{tr}\{\cdot\}$ and $\det\{\cdot\}$ calculate the trace and determinant of a matrix, respectively; $[X]_{i,\star}$ denotes the ith row of matrix X. We write random variables,

random vectors, and random matrices in sans serif, upright fonts as x, $\mathbf{x}$, and X, respectively. The notation $p(\boldsymbol{x})$ denotes the probability density function (PDF) $p_{\mathbf{x}}(\boldsymbol{x})$ of a random vector $\mathbf{x}$; $p(\boldsymbol{x}|\boldsymbol{y})$ denotes the conditional PDF $p_{\mathbf{x}|\mathbf{y}}(\boldsymbol{x}|\boldsymbol{y})$; $\mathbb{E}\{\cdot\}$ denotes the expectation operator. $\mathbf{x} \sim \mathcal{N}(\boldsymbol{\mu}, \boldsymbol{\Sigma})$ represents that random vector $\mathbf{x}$ follows Gaussian distribution with mean $\boldsymbol{\mu}$ and covariance matrix $\boldsymbol{\Sigma}$, and its PDF is denoted by $\mathcal{N}(\boldsymbol{x}; \boldsymbol{\mu}, \boldsymbol{\Sigma})$. $\mathcal{U}(\boldsymbol{a}, \boldsymbol{b})$ represents a uniform distribution from $\boldsymbol{a}$ to $\boldsymbol{b}$. Finally, the cardinality of a set $\mathcal{S}$ is denoted by $|\mathcal{S}|$.

2 RELATED WORKS

We briefly present related works on SAL and phase ambiguity resolution in this section. SAL is one of key research trends for reducing infrastructure requirement of localization systems, which can be simply divided into two categories: positioning using an anchor equipped with a single antenna and that with an antenna array.

With a single anchor equipped with single antenna, the position of the agent cannot be uniquely determined in general. Multiple measurements obtained by some means are required to locate the agent. One approach is to extract MPCs from the channel impulse response (CIR) measured by wideband signals. With known floor plan, authors in [31] turned physical anchor into a set of VAs by mirroring at the corresponding reflective surface. Such localization scheme was implemented on commercial UWB chips in [32]. Another approach is to locate agents with a single mobile anchor, where multiple measurements from the anchor with different positions are available. The agent is localized using a mobile anchor with known positions in [33] and a uniformly rotating anchor on a blade in [34].

When the anchor is equipped with an antenna array, AoA of a RF wave can be measured by distance differences between different array elements, which can be obtained by carrier phase of UWB [24], channel state information of Wi-Fi [14] or constant tone extension packets in Bluetooth 5.1 [15]. When the anchor does not have the ability to measure distance accurately, RSSI and MPCs [35] are utilized to achieve localization. Otherwise, with the ability of precise ranging, hybrid ToF/AoA localization scheme is commonly used. A SAL localization and synchronization scheme is proposed in [21] using full-duplex radios. In [22], a joint ToA/AoA estimator is proposed for impulse radio ultra-wideband (IR-UWB) localization using signal samples obtained at the Nyquist rate. A SAL system based on commercial UWB chips DecaWave DW1000 is developed in [23], which can achieve decimeter-level localization with a three-antenna anchor. By estimating AoA with UWB radios in a concurrent scheme, the efficiency of localization systems can be significantly improved [36].

AoA estimation algorithms can be divided into three categories, the maximum likelihood (ML) approach [37], classical estimation approaches such as the minimum variance distortionless response method [38], and subspace-based approaches including multiple signal classification [39] and estimation of signal parameters via rotational invariance technique [40]. These methods suffer from manifold ambiguity problem, which was studied in [41] using a general framework. A variety of methods have been proposed to resolve ambiguities. The first type focuses on the design of

array geometry. Several sparse array configurations with antenna spacings wider than half-wavelength have been proposed to improve the accuracy of AoA estimation without introducing angle ambiguity, including minimum-redundancy arrays [42], nested arrays [43] and co-prime arrays [44]. The second type resolves ambiguities using auxiliary hardwares, such as electromagnetic vector sensors [45] and planer substrates [46]. A rotary method by rotating the array was proposed to suppress ambiguity in [47]. The third type is resolving ambiguities by algorithms. Mapping measurements into outputs of a virtual array by interpolation can overcome the ambiguity problem [48]. The multi-scale method utilizes a coarse unambiguous estimation to disambiguate the fine AoA estimation [29]. Multiple target tracking algorithm was proposed in [28] to track paths of local peaks of likelihood function and the path with highest cumulative likelihood is selected as the "true" path.

Using PDoA measurements of a two-antenna commercial UWB device to estimate AoA was first proposed in [24]. Authors in [23] increased the quantity of antenna elements to achieve localization with a single anchor. We follow the technical route of [23] and further expand antenna spacings to reduce mutual coupling and improve localization accuracy. The proposed system has no strict restriction on array geometry compared to sparse array and has no auxiliary hardware. The position ambiguities are first encapsulated into SPI extracted from wrapped PDoA measurements, and are further resolved by multiple information fusion algorithms using coarse unambiguous TDoA measurements, inertial measurement unit (IMU), and map information.

3 SYSTEM OVERVIEW

The system architecture of the proposed single-anchor UWB localization system is shown in Fig. 1, which consists of *UWB measurement*, *soft positional information estimation* and *information fusion*, and discussed below:

1) *UWB Measurement*: Commercial UWB chips can measure high-precision CIR due to the impulse nature of UWB signals and the perfect periodic autocorrelation property of preamble signals [49]. Agents can be located by exchanging signals with a single UWB anchor equipped with an antenna array. The master antenna obtain distance measurements by alternative double-sided two-way ranging (ADS-TWR) method [50]. Meanwhile, all antennas receive the signal transmitted from the agent and measure CIR. Since several UWB frames are required by the ranging process of ADS-TWR method, multiple CIR measurements can be obtained to reduce measurement noise.

2) *Soft Positional Information Estimation* (Section 4): The first path of CIR is identified by the on-chip leading edge detection algorithm and refined by sinc interpolation. The time and phase of the first path in CIR are ToA and carrier phase of the received UWB signal respectively [24], which are used to estimate agents' position. When antenna spacings are above half wavelength, PDoA measurements are wrapped to $[-\pi, \pi]$, leading to phase ambiguity. To handle the
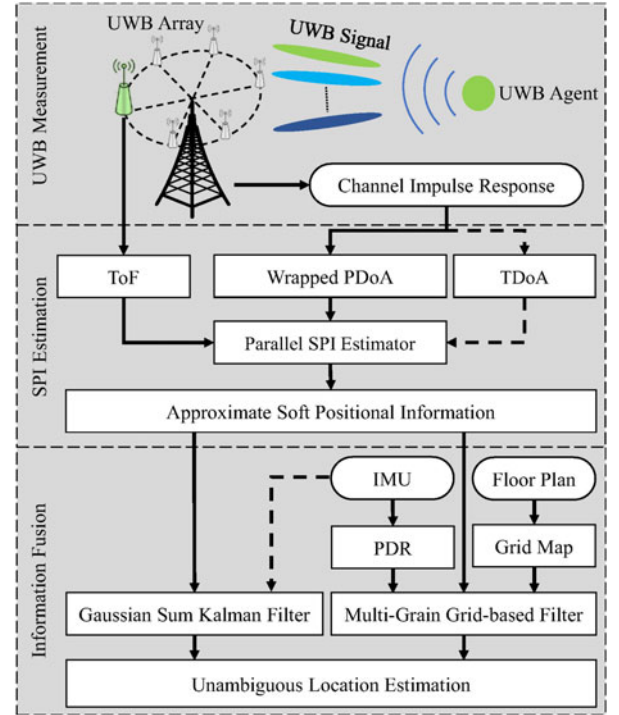

Fig. 1. System architecture.

phase wrapping problem, the GMM is used to approximate the SPI extracted from ambiguous measurements. A parallel SPI estimation algorithm is proposed to estimate parameters in GMM from wrapped PDoA measurements efficiently. Optionally, TDoA measurements can be incorporated into SPI to assist ambiguity resolution.

3) *Information Fusion* (Section 5): Due to large noises in TDoA measurements, location ambiguities cannot be resolved accurately. Hence, two tracking algorithms for different scenarios are proposed to track location ambiguities with SPI. In open spaces, the agent's movement is tracked by GSKF. In complex indoor environment, PDR measurements, floor plans and UWB measurements are fused by a multi-grain grid-based filter.

4 SOFT POSITIONAL INFORMATION ESTIMATION

In this section, we first present the system model and then derive the performance metric. Finally, a parallel SPI estimation algorithm is proposed to estimate parameters in approximate SPI represented by GMM efficiently.

4.1 Problem Formulation

We consider a UWB SAL system where there is an agent and a single anchor equipped with an M-element array in a 3D space. The position of each antenna of the anchor is precisely known and the unknown agent's position is determined by exchanging signals with the anchor. The anchor can perform ranging with the agent on the master antenna using ADS-TWR method [50]. Meanwhile, all antennas of the anchor receive signals transmitted by the agent simultaneously and estimate CIRs, from which ToAs and PoAs can be extracted.

Let $\boldsymbol{p} = [p_x, p_y, p_z]^T \in \mathbb{R}^3$ and $\boldsymbol{q}_i = [q_{ix}, q_{iy}, q_{iz}]^T \in \mathbb{R}^3$ ($1 \leq i \leq M$) denote the agent's position and the position of the ith antenna, respectively. Then, the distance between agent and ith antenna is given by

$$\mathcal{D}(\boldsymbol{p}, \boldsymbol{q}_i) = \sqrt{(p_x - q_{ix})^2 + (p_y - q_{iy})^2 + (p_z - q_{iz})^2}.$$

By exchanging several UWB frames, the distance between agent and the first antenna can be measured by ADS-TWR method [50], which is

$$\mathsf{d} = \mathcal{D}(\boldsymbol{p}, \boldsymbol{q}_1) + \mathsf{n}_d, \tag{1}$$

where $\mathsf{n}_d \sim \mathcal{N}(0, \sigma_d^2)$ is the noise of distance measurements.

In the process of ranging, all antennas of the anchor receive signals transmitted by the agent simultaneously and provide ToA and PoA estimations, which is

$$\mathsf{t}_i = \frac{1}{c}\mathcal{D}(\boldsymbol{p}, \boldsymbol{q}_i) + \Delta t + \mathsf{n}_{t_i} \tag{2}$$

$$\theta_i = -\frac{2\pi f_c}{c}\mathcal{D}(\boldsymbol{p}, \boldsymbol{q}_i) + \Delta \theta + \mathsf{n}_{\vartheta_i}, \; i = 1, 2, \ldots, M, \tag{3}$$

where f_c is the carrier frequency and c is the speed of light; $\mathsf{n}_{t_i} \sim \mathcal{N}(0, \sigma_{t_i}^2)$ and $\mathsf{n}_{\vartheta_i} \sim \mathcal{N}(0, \sigma_{\vartheta_i}^2)$ are the noise of ToA and PoA measurements respectively, the variances of which are assumed to be known; Δt and $\Delta \theta$ are time and phase offset between clocks of the anchor and agent, which can be eliminated when all antennas are clock synchronized. If we take t_1 and θ_1 as reference, TDoA measurements $\boldsymbol{\tau} = [\tau_1, \tau_2, \ldots, \tau_{M-1}]^T$ and PDoA measurements $\boldsymbol{\varphi} = [\varphi_1, \varphi_2, \ldots, \varphi_{M-1}]^T$ are given by

$$\boldsymbol{\tau} = C[\mathsf{t}_1, \mathsf{t}_2, \ldots, \mathsf{t}_M]^T, \;\; \boldsymbol{\varphi} = C[\theta_1, \theta_2, \ldots, \theta_M]^T,$$

where $C = [-\mathbf{1}_{M-1}, \boldsymbol{I}_{M-1}]$ is a transformation matrix. The noise of TDoA and PDoA measurements are given by

$$\mathsf{n}_\tau \sim \mathcal{N}(0, \boldsymbol{\Sigma}_\tau), \; \mathsf{n}_\varphi \sim \mathcal{N}(0, \boldsymbol{\Sigma}_\varphi),$$

where

$$\boldsymbol{\Sigma}_\tau = C\text{diag}([\sigma_{t_1}^2, \sigma_{t_2}^2, \ldots, \sigma_{t_M}^2])C^T$$
$$\boldsymbol{\Sigma}_\varphi = C\text{diag}([\sigma_{\vartheta_1}^2, \sigma_{\vartheta_2}^2, \ldots, \sigma_{\vartheta_M}^2])C^T.$$

are covariance matrices of TDoA and PDoA noise. The goal of the localization problem is to determine the agent's position $\boldsymbol{p} \in \mathbb{R}^3$ from all measurements $\mathbf{y} = [\mathsf{d}; \boldsymbol{\tau}; \boldsymbol{\varphi}]$.

4.2 Performance Metric

The lower bound of mean square error (MSE) of any unbiased location estimator is given by the SPEB [51], which is adopted as performance metric to characterize the localization accuracy of the proposed localization system. For an unknown agent's position $\boldsymbol{p}$, the SPEB is defined as

$$\mathbb{E}\{\|\hat{\boldsymbol{p}} - \boldsymbol{p}\|^2\} \geq \text{SPEB}(\boldsymbol{p}) \triangleq \text{tr}\{\boldsymbol{J}^{-1}(\boldsymbol{p})\},$$

where $\boldsymbol{J}(\boldsymbol{p})$ is the Fisher information matrix (FIM) [52].

All measurements related to the agent's position $\boldsymbol{p}$ consist of a distance measurement d, $M - 1$ TDoA measurements $\boldsymbol{\tau}$ and $M - 1$ PDoA measurements $\boldsymbol{\varphi}$, which are represented by $\mathbf{y} = [\mathsf{d}; \boldsymbol{\tau}; \boldsymbol{\varphi}]$. Then, the FIM for the agent's position $\boldsymbol{p}$ is given by

$$\boldsymbol{J}(\boldsymbol{p}) = -\mathbb{E}\left\{ \frac{\partial^2 \ln p(\boldsymbol{y}; \boldsymbol{p})}{\partial \boldsymbol{p} \partial \boldsymbol{p}^T} \right\}. \tag{4}$$

Proposition 1. *The FIM for the agent's position $\boldsymbol{J}(\boldsymbol{p})$ using distance, TDoA and PDoA measurements can be described as*

$$\boldsymbol{J}(\boldsymbol{p}) = \boldsymbol{J}_\mathsf{d}(\boldsymbol{p}) + \boldsymbol{J}_\tau(\boldsymbol{p}) + \boldsymbol{J}_\varphi(\boldsymbol{p}),$$

where

$$\boldsymbol{J}_\mathsf{d}(\boldsymbol{p}) = \frac{1}{\sigma_d^2} \frac{\partial \mathcal{D}(\boldsymbol{p}, \boldsymbol{q}_1)}{\partial \boldsymbol{p}} \frac{\partial \mathcal{D}(\boldsymbol{p}, \boldsymbol{q}_1)}{\partial \boldsymbol{p}^T}, \tag{5}$$

$$\boldsymbol{J}_\tau(\boldsymbol{p}) = \frac{1}{c^2} \boldsymbol{T}(\boldsymbol{p})^T \boldsymbol{C}^T \boldsymbol{\Sigma}_\tau^{-1} \boldsymbol{C}\boldsymbol{T}(\boldsymbol{p}), \tag{6}$$

$$\boldsymbol{J}_\varphi(\boldsymbol{p}) = \frac{4\pi^2 f_c^2}{c^2} \boldsymbol{T}(\boldsymbol{p})^T \boldsymbol{C}^T \boldsymbol{\Sigma}_\varphi^{-1} \boldsymbol{C}\boldsymbol{T}(\boldsymbol{p}), \tag{7}$$

and

$$\boldsymbol{T}(\boldsymbol{p}) = \frac{\partial \boldsymbol{\mathcal{D}}(\boldsymbol{p})}{\partial \boldsymbol{p}^T} = \begin{bmatrix} \frac{p_x - q_{1x}}{\mathcal{D}(\boldsymbol{p}, \boldsymbol{q}_1)} & \frac{p_y - q_{1y}}{\mathcal{D}(\boldsymbol{p}, \boldsymbol{q}_1)} & \frac{p_z - q_{1z}}{\mathcal{D}(\boldsymbol{p}, \boldsymbol{q}_1)} \\ \vdots & \vdots & \vdots \\ \frac{p_x - q_{Mx}}{\mathcal{D}(\boldsymbol{p}, \boldsymbol{q}_M)} & \frac{p_y - q_{My}}{\mathcal{D}(\boldsymbol{p}, \boldsymbol{q}_M)} & \frac{p_z - q_{Mz}}{\mathcal{D}(\boldsymbol{p}, \boldsymbol{q}_M)} \end{bmatrix}$$
$$\boldsymbol{\mathcal{D}}(\boldsymbol{p}) = [\mathcal{D}(\boldsymbol{p}, \boldsymbol{q}_1), \ldots, \mathcal{D}(\boldsymbol{p}, \boldsymbol{q}_M)]^T.$$

Proof. Since noises of d, $\boldsymbol{\tau}$ and $\boldsymbol{\varphi}$ are mutually independent,[1] the overall information is the sum of information from each measurement. We can obtain the FIM for the agent's position $\boldsymbol{J}(\boldsymbol{p})$ according to (4). □

Remark 1. The FIM in (7) demonstrates that the localization accuracy can be improved by using higher carrier frequency f_c. Intuitively, when the noise of PDoA measurements remain unchanged, a higher carrier frequency means a shorter wavelength, and PDoA errors correspond to smaller distance difference errors. In addition, TDoA measurements are of little help in improving localization accuracy compared to PDoA measurements.[2]

Remark 2. The localization accuracy can be improved by expanding antenna spacings, but which will introduce the phase wrapping problem. Assuming that the agent is far from the anchor, distances between the agent and each antenna of the anchor are almost equal. Therefore,

$$[\boldsymbol{C}\boldsymbol{T}(\boldsymbol{p})]_{i-1,\star} = [\boldsymbol{T}(\boldsymbol{p})]_{i,\star} - [\boldsymbol{T}(\boldsymbol{p})]_{1,\star}$$
$$\approx \left[\frac{q_{1x} - q_{ix}}{\mathcal{D}(\boldsymbol{p}, \boldsymbol{q}_1)}, \frac{q_{1y} - q_{iy}}{\mathcal{D}(\boldsymbol{p}, \boldsymbol{q}_1)}, \frac{q_{1z} - q_{iz}}{\mathcal{D}(\boldsymbol{p}, \boldsymbol{q}_1)} \right],$$

---

1. We assume that noises in measurements of distance, ToAs, and PoAs are independent, since main errors in these measurements are from clock drift, analog-to-digital converter sampling error, and carrier recovery in real system, respectively.
2. The typical value of σ_t and σ_ϑ are 80 ps and $3°$ respectively, which correspond to 2.4 cm and 0.06 cm at $f_c = 4$ GHz. Thus, (6) is about 1,600 times larger than (7), which is negligible in $\boldsymbol{J}^{-1}(\boldsymbol{p})$.

indicating that the localization accuracy is proportional to antenna spacings. The FIMs in (6) and (7) will increase with the antenna spacing.

4.3 SPI Estimation With Wrapped PDoA

We first model the wrapped PDoA, and then present the definition of SPI, followed by the proposed parallel SPI estimation algorithm handling the phase wrapping problem.

When antenna spacings are larger than half-wavelength, PDoA measurements are wrapped to $[-\pi, \pi]$, that is,

$$\tilde{\varphi}_i = \varphi_i - 2s_i\pi, \ s_i \in \mathbb{Z}.$$

The log-likelihood function with PDoA ambiguities is

$$\ell(\boldsymbol{p}) = \ln p(\hat{\boldsymbol{y}}; \boldsymbol{p}) = \ell_{\mathsf{d}}(\boldsymbol{p}) + \ell_{\boldsymbol{\tau}}(\boldsymbol{p}) + \ell_{\tilde{\varphi}}(\boldsymbol{p}), \qquad (8)$$

and

$$\ell_{\mathsf{d}}(\boldsymbol{p}) = \text{const.} - \frac{(\hat{d} - \mathcal{D}(\boldsymbol{p}, \boldsymbol{q}_1))^2}{2\sigma_d^2}$$

$$\ell_{\boldsymbol{\tau}}(\boldsymbol{p}) = \text{const.} - \left(\hat{\boldsymbol{\tau}} - \frac{1}{c}C\mathcal{D}(\boldsymbol{p})\right)^{\mathrm{T}} \boldsymbol{\Sigma}_{\tau}^{-1} \left(\hat{\boldsymbol{\tau}} - \frac{1}{c}C\mathcal{D}(\boldsymbol{p})\right)$$

$$\ell_{\tilde{\varphi}}(\boldsymbol{p}) = \text{const.}$$
$$- \mathcal{W}\left(\hat{\tilde{\boldsymbol{\varphi}}} + \frac{2\pi f_{\mathrm{c}}}{c}C\mathcal{D}(\boldsymbol{p})\right)^{\mathrm{T}} \boldsymbol{\Sigma}_{\varphi}^{-1} \mathcal{W}\left(\hat{\tilde{\boldsymbol{\varphi}}} + \frac{2\pi f_{\mathrm{c}}}{c}C\mathcal{D}(\boldsymbol{p})\right),$$

where $\hat{\boldsymbol{y}} = [\hat{d}; \hat{\boldsymbol{\tau}}; \hat{\tilde{\boldsymbol{\varphi}}}]$ are measurements with PDoA ambiguities and $\mathcal{W}(\cdot)$ wraps angles to $[-\pi, \pi]$. The ML estimation of agent's position cannot be solved by the gradient descent method because $\mathcal{W}(\cdot)$ is non-convex. Moreover, ambiguous PDoA measurements result in ambiguous position estimates. Traditional ML estimator can only solve the position with the highest probability, which may be incorrect because of PDoA ambiguities and measurement noise.

To retain statistical characteristics of ambiguous measurements, we exploit *soft positional information*.

Definition 1 (SPI [30]). *We define the SPI of a measurement* $\boldsymbol{y} = \hat{\boldsymbol{y}}$, *denoted by* $\mathcal{L}_{\boldsymbol{y}}(\boldsymbol{p})$, *to be a function of agent's position* $\boldsymbol{p}$ *proportional to* $p(\hat{\boldsymbol{y}}; \boldsymbol{p})$, *i.e.,* $\mathcal{L}_{\boldsymbol{y}}(\boldsymbol{p}) \propto p(\hat{\boldsymbol{y}}; \boldsymbol{p})$.

Considering that the likelihood function (8) with phase ambiguities is multimodal, we use GMM to approximate the SPI with PDoA ambiguities, given by

$$\mathcal{L}_{\boldsymbol{y}}(\boldsymbol{p}) \propto p(\hat{\boldsymbol{y}}; \boldsymbol{p}) \approx \sum_{l=1}^{L} \beta^l \mathcal{N}(\boldsymbol{p}; \hat{\boldsymbol{p}}_{\mathrm{ML}}^l, \boldsymbol{\Sigma}^l), \qquad (9)$$

where $\{\beta^l, \hat{\boldsymbol{p}}_{\mathrm{ML}}^l, \boldsymbol{\Sigma}^l\}_{l=1}^{L}$ are parameters of GMM. Different superscript l corresponds to different ambiguities, which are resolved later. First, the center of each component represents a possible position, which is estimated by ML algorithm

$$\hat{\boldsymbol{p}}_{\mathrm{ML}}^l = \arg\max_{\boldsymbol{p}} \ \ell(\boldsymbol{p}; \boldsymbol{s}^l),$$

where $\boldsymbol{s} = [s_1, s_2, \ldots, s_{M-1}]^{\mathrm{T}}$ denote PDoA ambiguities. By replacing ambiguous PDoA measurements $\hat{\tilde{\boldsymbol{\varphi}}}$ with absolute PDoA values $\hat{\tilde{\boldsymbol{\varphi}}} + 2\pi \boldsymbol{s}^l$, the ML estimation can be obtained by maximizing (8) without $\mathcal{W}(\cdot)$ using gradient descent method. Then, the covariance matrix of lth component $\boldsymbol{\Sigma}^l$ is approximated by sampling around $\hat{\boldsymbol{p}}_{\mathrm{ML}}^l$, given by

$$\boldsymbol{\Sigma}^l = \sum_{i=1}^{N_s} w_{l,i} (\boldsymbol{p}^{l,i} - \hat{\boldsymbol{p}}_{\mathrm{ML}}^l)(\boldsymbol{p}^{l,i} - \hat{\boldsymbol{p}}_{\mathrm{ML}}^l)^{\mathrm{T}} \qquad (10)$$

$$w_{l,i} \propto p(\hat{\boldsymbol{y}}; \boldsymbol{p}^{l,i}, \boldsymbol{s}^l), \qquad (11)$$

where N_s is the number of sampling points. $\boldsymbol{p}^{l,i}$ is the ith sampling point around $\hat{\boldsymbol{p}}_{\mathrm{ML}}^l$ and $w_{l,i}$ is normalized such that they sum up to one. Finally, the weight of the lth Gaussian component is

$$\beta^l \propto p(\hat{\boldsymbol{y}}; \hat{\boldsymbol{p}}_{\mathrm{ML}}^l, \boldsymbol{s}^l)\sqrt{\det\{\boldsymbol{\Sigma}^l\}}, \qquad (12)$$

which keeps the ratio between the maximum probabilities of each component unchanged. The approximate SPI in (9) can retain statistical characteristics of measurements while has low computational complexity in the filtering process.

A parallel SPI estimation algorithm is proposed to estimate parameters of approximate SPI efficiently. The proposed algorithm consists of two steps: first, searching all possible ambiguities; second, approximating parameters of Gaussian components for each ambiguity.

1) *Ambiguity Searching*: Assuming that the distance between antennas is $N_d\lambda/2$, it is inefficient to calculate all N_d^{M-1} pair-wise ambiguities by exhaustive method. The proposed algorithm obtains valid ambiguities by searching local maximums of the log-likelihood function in (8) on a sphere triangle mesh with radius $\hat{d}$ in parallel, which is expressed as

$$\hat{\boldsymbol{p}}^1, \hat{\boldsymbol{p}}^2, \ldots, \hat{\boldsymbol{p}}^L = \arg(\text{local})\max_{\boldsymbol{p}} \ell(\boldsymbol{p}).$$

Each local maximum point corresponds to a valid ambiguity, which is calculated by

$$\boldsymbol{s}^l = \frac{1}{2\pi}\left(\frac{2\pi f_{\mathrm{c}}}{c}C\mathcal{D}(\hat{\boldsymbol{p}}^l) - \hat{\tilde{\boldsymbol{\varphi}}}\right). \qquad (13)$$

In addition, repeated ambiguities should be removed.

2) *SPI Approximation*: After obtaining all valid ambiguities, we find ML estimation of agent's position for each ambiguity by grid searching around $\hat{\boldsymbol{p}}^l$, which is easier to parallelize than gradient method. Then the covariance matrix of lth component $\boldsymbol{\Sigma}^l$ is approximated by sampling around $\hat{\boldsymbol{p}}_{\mathrm{ML}}^l$ using (10), (11) and the weight β^l is calculated by (12). Finally, components with small weight are removed.

We summarize the overall algorithm in Algorithm 1. The computational complexity of the proposed algorithm is $\mathcal{O}(M^3|\mathcal{V}|) + \mathcal{O}(M^3(N_g + N_s)|\mathcal{P}|)$. The computational complexity of calculating the log-likelihood function is $\mathcal{O}(M^3)$ and N_g is the number of grid points while finding ML estimation. The sphere triangle mesh can be generated in advance, which is not included in the computational complexity. Almost all steps in Algorithm 1 can be accelerated by parallel computing, which allows the algorithm to calculate the positioning results in real time.

Note that TDoA measurements are not the most critical component in Algorithm 1, which can be omitted by removing $\ell_{\boldsymbol{\tau}}(\boldsymbol{p})$ from (8). However, when TDoA measurements are

Algorithm 1. Parallel Soft Positional Information Estimation

Input:
 The position of antennas q_i, $i = 1, 2, \ldots, M$;
 Distance measurement $\hat{d}$;
 TDoA measurements $\hat{\tau}$;
 Wrapped PDoA measurements $\hat{\bar{\varphi}}$;
Output:
 Approximate SPI parameters $(\beta^l, \hat{p}_{\text{ML}}^l, \Sigma^l)_{l=1}^L$;
 1: *1) Ambiguity Searching:*
 2: Generate a sphere triangle mesh $\mathcal{V}$;
 3: Calculate (8) **in parallel** for all points in $\mathcal{V}$;
 4: Find local maximums of (8) **in parallel**, denoted by $\mathcal{P}$;
 5: Calculate corresponding ambiguities according to (13);
 6: Remove repeated ambiguities;
 7: *2) SPI Approximation:*
 8: **for** all $\hat{p}^l \in \mathcal{P}$ **do**
 9:     Find the ML estimation of position $\hat{p}_{\text{ML}}^l$ by maximizing $\ell(p; s^l)$ by grid searching **in parallel**;
10:     Sample around $\hat{p}_{\text{ML}}^l$ and calculate (11) **in parallel**;
11:     Calculate the covariance matrix Σ^l by reduction algorithm **in parallel** according to (10);
12:     Calculate β^l according to (12);
13: **end for**
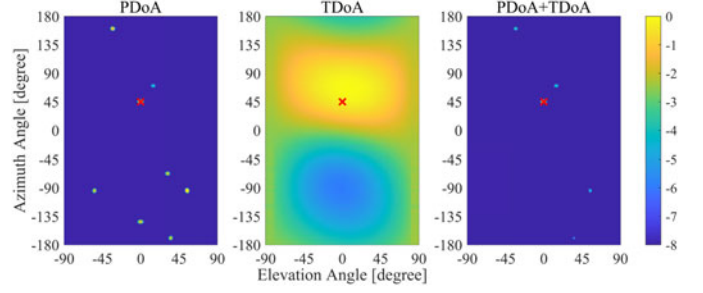14: Remove components with small weight.

Fig. 2. Log-likelihood function of agent's position using PDoA, TDoA and PDoA+TDoA measurements. The true azimuth and elevation angle of the agent is marked as a red cross.

available, they can provide significant help for ambiguity resolution, which is validated through a simulation. The anchor consists of four antennas in a pyramid shape and the bottom side is 20 cm and the height is 9 cm. The agent is placed at (15 m, 15 m, 0 m) and carrier frequency is 4 GHz. Log-likelihood function of PDoA, TDoA and PDoA+TDoA measurements are shown in Fig. 2. The result shows that TDoA can resolve most location ambiguities, but there are still some ambiguities due to the low accuracy of TDoA, which can be resolved by information fusion.

5 INFORMATION FUSION

This section describes information fusion methods exploiting SPI extracted from raw measurements with phase ambiguities. We first present the recursive Bayesian filtering framework to resolve location ambiguities. Then two cases are studied, which are 3D positioning in open space and 2D pedestrian positioning in complex indoor environments.

5.1 Recursive Bayesian Filtering Framework

The localization problem can be represented by a sequence of discrete time variables $(\mathbf{x}_k, \mathbf{m}_k, \mathbf{y}_k)$, where $\mathbf{x}_k$ denotes the state vector including position and other states of agents, $\mathbf{y}_k$ denotes UWB measurements with PDoA ambiguities at time k, and $\mathbf{m}_k$ denotes IMU measurements. Hence, localization problem is to estimate locations given UWB measurements and IMU measurements, formulated as

$$\mathbf{x}_k = \boldsymbol{f}(\mathbf{x}_{k-1}, \mathbf{m}_k, \mathbf{w}_k) \tag{14}$$

$$\mathbf{y}_k = \boldsymbol{h}_k(\mathbf{x}_k, \mathbf{v}_k), \tag{15}$$

where the location estimation is predicted by transition model $\boldsymbol{f}(\cdot)$ and updated by observation model $\boldsymbol{h}_k(\cdot)$; $\mathbf{w}_k$ and $\mathbf{v}_k$ are process noise and observation noise respectively. The SPI of UWB measurements with phase ambiguities is approximated by GMM, as shown in (9), parameters of which are estimated by Algorithm 1.

The recursive Bayesian filter consists of prediction step and update step, which can solve the localization problem defined in (14) and (15). In prediction step, the state transition model (14) is used to predict the prior PDF $p(\boldsymbol{x}_k|\boldsymbol{y}_{1:k-1})$ at time k. In update step, the observation model (15) is used to update the posterior PDF $p(\boldsymbol{x}_k|\boldsymbol{y}_{1:k})$. Therefore, we can calculate the posterior PDF of each time recursively by

$$p(\boldsymbol{x}_k|\boldsymbol{y}_{1:k-1}) \propto \int p(\boldsymbol{x}_k|\boldsymbol{x}_{k-1}, \boldsymbol{m}_k)p(\boldsymbol{x}_{k-1}|\boldsymbol{y}_{1:k-1})\mathrm{d}\boldsymbol{x}_{k-1} \tag{16}$$

$$p(\boldsymbol{x}_k|\boldsymbol{y}_{1:k}) \propto p(\boldsymbol{y}_k|\boldsymbol{x}_k)p(\boldsymbol{x}_k|\boldsymbol{y}_{1:k-1}). \tag{17}$$

The system models are often non-linear and non-Gaussian in practice, which makes it difficult to describe the PDF in analytical expressions. In this paper, two approximation methods of the PDF are proposed for different scenarios. For the scenario of 3D positioning in open space, GMM is used to describe PDFs of state variables, as shown in Section 5.2. For the scenario of 2D pedestrian positioning in complex indoor environments, the PDF is approximated by a set of discrete states in order to fuse map information efficiently, as shown in Section 5.3.

5.2 Gaussian Sum Kalman Filtering Algorithm

In a space without obstacles, transition of location probability is linear and the observation likelihood is approximated by GMM. Therefore, it is natural to track the movement of agents by a GSKF, which is able to resolve location ambiguities and improve the localization accuracy.

We define the system state as $\mathbf{x}_k = [\mathbf{p}_k; \dot{\mathbf{p}}_k]$ including position and velocity. The transition model (14) is given by

$$\mathbf{x}_k = A\mathbf{x}_{k-1} + G_k\mathbf{m}_k + \mathbf{w}_k, \tag{18}$$

where

$$A = \begin{bmatrix} I_{3\times3} & \Delta t I_{3\times3} \\ 0_{3\times3} & I_{3\times3} \end{bmatrix},$$

and $\mathbf{w}_k \sim \mathcal{N}(0, Q_k)$ is the process noise. The observation likelihood in (15) is calculated by Algorithm 1 and given by

$$p(\boldsymbol{y}_k|\boldsymbol{x}_k) \propto \mathcal{L}_{\mathbf{y}_k}(H\boldsymbol{x}_k) \approx \sum_{l=1}^{L_k} \beta_k^l \mathcal{N}(H\boldsymbol{x}_k; \hat{\boldsymbol{p}}_{\mathrm{ML},k}^l, \boldsymbol{\Sigma}_k^l), \tag{19}$$

where

$$H = [I_{3\times3}, 0_{3\times3}].$$

When the agent is equipped with IMU, changes in velocity can be measured by integrating transformed accelerations in the world coordinate system (WCS) over time. And the noise is assumed to be Gaussian distributed. Therefore,

$$\mathbf{m}_k \sim \mathcal{N}(\hat{m}_k, \boldsymbol{\Sigma}_{v,k})$$
$$G_k = [0.5\Delta t I_{3\times3}, I_{3\times3}]^{\mathrm{T}}.$$

When IMU is unavailable, location ambiguities can also be resolved since TDoA measurements are unambiguous. In this case, the movement of agents is assumed to be a Markov random movement, i.e., the term $G_k\mathbf{m}_k$ in (18) is omitted.

The PDF of $\mathbf{x}_k$ is approximated by GMM

$$p(\boldsymbol{x}_k|\boldsymbol{y}_{1:k}) \approx \sum_{i=1}^{N_{k|k}} \alpha_{k|k}^i \mathcal{N}(\boldsymbol{x}_k; \hat{\boldsymbol{x}}_{k|k}^i, P_{k|k}^i), \tag{20}$$

where the ith component is characterized by Gaussian distribution with weight $\alpha_{k|k}^i$, mean $\hat{\boldsymbol{x}}_{k|k}^i$ and covariance matrix $P_{k|k}^i$. Only those components with weights larger than a threshold are preserved and weights are normalized such that $\sum_{i=1}^{N_{k|k}} \alpha_{k|k}^i = 1$. Then, by substituting (20) into (16), the prediction step is given by

$$\hat{\boldsymbol{x}}_{k|k-1}^i = A\hat{\boldsymbol{x}}_{k-1|k-1}^i + G_k\hat{m}_k$$
$$P_{k|k-1}^i = AP_{k-1|k-1}^i A^{\mathrm{T}} + G_k\boldsymbol{\Sigma}_{v,k}G_k^{\mathrm{T}} + Q_k, \tag{21}$$

and

$$N_{k|k-1} = N_{k-1|k-1}, \quad \alpha_{k|k-1}^i = \alpha_{k-1|k-1}^i. \tag{22}$$

By substituting (19) and (20) into (17), the update step is given by

$$z_k^j = \hat{\boldsymbol{p}}_{\mathrm{ML},k}^l - H\hat{\boldsymbol{x}}_{k|k-1}^i$$
$$S_k^j = HP_{k|k-1}^i H^{\mathrm{T}} + \boldsymbol{\Sigma}_k^l$$
$$K_k^j = P_{k|k-1}^i H^{\mathrm{T}}(S_k^j)^{-1} \tag{23}$$
$$\hat{\boldsymbol{x}}_{k|k}^j = \hat{\boldsymbol{x}}_{k|k-1}^i + K_k^j z_k^j$$
$$P_{k|k}^j = (I - K_k^j H)P_{k|k-1}^i,$$

Algorithm 2. Gaussian Sum Kalman Filtering

Input:
    IMU measurements, $\mathbf{m}_k$;
    Approximate observation likelihood function parameters from Algorithm 1, $\{\beta^l, \hat{\boldsymbol{p}}_{\mathrm{ML}}^l, \boldsymbol{\Sigma}^l\}_{l=1}^{N_a}$;
Output:
    Estimated locations, $\hat{\mathbf{x}}_{k|k}$;
1: Initialize by UWB measurements;
2: **for** $k = 2 : T$ **do**
3:     Predict $\hat{\mathbf{x}}_{k|k-1}$ according to (21) and (22);
4:     **if** UWB measurements is valid **then**
5:       Update $\hat{\mathbf{x}}_{k|k}$ according to (23) and (24);
6:     **else**
7:       $\hat{\mathbf{x}}_{k|k} = \hat{\mathbf{x}}_{k|k-1}$;
8:     **end if**
9:     Calculate estimated location $\hat{\mathbf{x}}_{k|k}$;
10:    Remove Gaussian components with small weight
11: **end for**

---

where

$$j = (i - 1)L_k + l$$
$$N_{k|k} = N_{k|k-1}L_k$$
$$\alpha_{k|k}^j = \frac{\alpha_{k|k-1}^i \beta_k^l \exp\left(-0.5(z_k^j)^{\mathrm{T}}(S_k^j)^{-1}z_k^j\right)}{(2\pi)^{1.5}\det\{S_k^j\}^{0.5}}. \tag{24}$$

The initial state of GSKF is obtained by the first UWB measurement. Then, IMU estimates the target pose and calculates the velocity of the agent continuously. When a new UWB measurement comes, IMU outputs the changes in agent's velocity and the GSKF predicts the agent's state. The observation likelihood function of UWB measurement is first approximated by Algorithm 1 and then used to update the position and velocity of the agent. The mean value of the Gaussian component with highest weight is chosen as the estimated location $\hat{\mathbf{x}}_{k|k}$. The overall algorithm is summarized in Algorithm 2.

5.3 Multi-Grained Grid-Based Filtering Algorithm

In complex indoor environments, localization accuracy of UWB system is heavily influenced by non-line-of-sight (NLOS) propagations. To reduce these effects, a large quantity of UWB anchors is required to keep users in line-of-sight (LOS) condition. We propose a multi-grained grid-based filter to fuse information from floor plans, PDR and UWB measurements, which can resolve location ambiguities, improve localization accuracy and reduce the number of UWB anchors required.

5.3.1 Map Discretization

Taking full advantage of map information can significantly improve the accuracy of PDR-based localization systems. Obstacles in indoor environments will restrict the movement of pedestrians and help eliminate impossible locations and movements. However, complex indoor environments make the state transition model in (14) non-linear and non-Gaussian. We subdivide the PDF of state variable into a
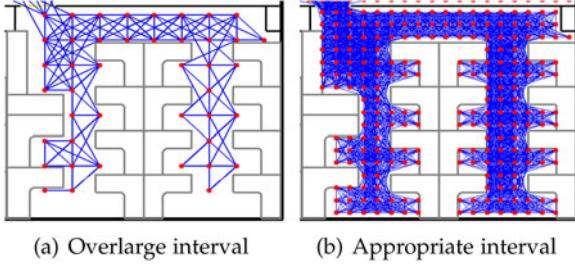
Fig. 3. Grid map with different quantization intervals. (a) shows overlarge quantization intervals will make narrow locations unreachable. (b) shows the result of discretized map with an appropriate quantization interval.

deterministic discrete grid and perform the recursive Bayesian filtering process on the discrete grid. In order to utilize map information efficiently, a grid-based map discretization algorithm with constraints on grid connectivity is proposed, which preprocesses the floor plan into a grid map.

Considering map constraints, the system model in (14) and (15) is non-linear and non-Gaussian and PDFs of state variables cannot be expressed in analytical expressions. Therefore, we discretize the continuous state space into N_p uniform grids $\{x^{(i_p)}\}_{i_p=1}^{N_p}$ to approximate PDFs by weights on grid points. Then, the transition of probabilities between grid points are limited by map constraints. Two grid points are connected only if the distance between two grid points is smaller than $d_{\max}$ and the segment does not intersect with obstacles, which can be expressed as

$$M(x^{(i_p)} \rightarrow x^{(j_p)}) = \begin{cases} 0, & \text{intersections between } i_p \text{ and } j_p \\ 0, & ||x^{(i_p)} - x^{(j_p)}|| > d_{\max} \\ 1, & \text{otherwise} \end{cases}.$$

The quantization interval should be chosen appropriately by considering the correctness, the accuracy of observations and computational complexity. Overlarge quantization intervals make narrow locations unreachable, as shown at the bottom of Fig. 3a. When fusing high-precision observation information, increasing quantization intervals will reduce the approximation accuracy of the observation likelihood function, which will affect the localization accuracy. On the contrary, decreasing quantization intervals will increase the computational and memory complexity quickly. It is worth mentioning that inappropriately decreasing quantization intervals cannot improve the localization accuracy significantly, because the filtering algorithm has compensated the quantization error which will be explained below. Taking all the factors into account, 0.4 m is an appropriate quantization interval, as shown in Fig. 3b.

5.3.2 Multi-Grained Grid-Based Filters

In PDR-based localization system, the localization problem is modeled as discrete time variables $((x_k, \theta_k), m_k, y_k)$ divided by the incident of steps. The error of heading direction is the main error source of PDR-based localization system. Therefore, the heading direction θ_k is estimated jointly with the position x_k. m_k denotes measurements of PDR algorithm and y_k represents UWB measurements.

PDR algorithm takes measurements of IMU as inputs, including step detection, stride length estimation and

---

Algorithm 3. Multi-Grained Grid-Based Filter

Input:
    Measurements from PDR component, m_k;
    Approximate observation likelihood function parameters from Algorithm 1, $\{\beta^l, \hat{p}_{\mathrm{ML}}^l, \Sigma^l\}_{l=1}^{N_a}$;

Output:
    Estimated locations, $\hat{\mathbf{x}}_{k|k}$;

1: Initialize by UWB measurements;
2: **for** $k = 2 : T$ **do**
3:    *Grid Weights Predict:*
4:    Calculate (33) for all possible direction;
5:    Predict weights according to (29);
6:    Remove those coarse grids with small weight
7:    Calculate estimated location $\hat{\mathbf{x}}_{k|k-1}$;
8:    *Grid Weights Update:*
9:    **if** UWB measurements is valid **then**
10:     Obtain $p(y_k|x_k; \mathrm{map})$ according to (27);
11:     Update weights according to (30);
12:     Remove those coarse grids with small weight
13:     Calculate estimated location $\hat{\mathbf{x}}_{k|k}$;
14:    **else**
15:     $\hat{\mathbf{x}}_{k|k} = \hat{\mathbf{x}}_{k|k-1}$;
16:    **end if**
17:    Calculate estimated location $\hat{\mathbf{x}}_{k|k}$;
18: **end for**

---

heading determination. We exploit periodic characteristics in acceleration to detect pedestrians' steps. Amplitude and time interval constraints of each step are added to reduce over-counting caused by noise. The stride length of each step is calculated by frequency model [53], which is commonly used and defined as $\widehat{SL}_k = a \cdot f + b$, where f is the step frequency. The stride length SL_k is assumed to follow uniform distribution $\mathcal{U}(\widehat{SL}_k - \Delta SL, \widehat{SL}_k + \Delta SL)$. Heading direction is estimated by a complementary filter [54] which can avoid the bias of gyroscope and reduce the susceptibility to ferromagnetic interference. The changes in heading direction are used as the input of filter, the error of which is assumed to follow Gaussian distribution $\mathcal{N}(0, \sigma_\vartheta^2)$. Therefore, measurements of PDR algorithm m_k consist of stride length SL_k and change of heading direction $\Delta \theta_k$.

Physical constraints in map information will limit the transition of location probabilities and help distinguish whether UWB measurements are in LOS or NLOS propagation conditions. After introducing map information, the system model described in (14) and (15) becomes

$$(\mathbf{x}_k, \theta_k) = f((\mathbf{x}_{k-1}, \theta_{k-1}), m_k, \mathbf{w}_k; \mathrm{map})$$
$$\mathbf{y}_k = h_k(\mathbf{x}_k, \mathbf{v}_k; \mathrm{map}),$$

and the prediction step and update step of the recursive Bayesian filter are given by

$$p(x_k, \vartheta_k | y_{1:k-1}) \propto \int p(x_k, \vartheta_k | x_{k-1}, \vartheta_{k-1}, m_k)$$
$$M(x_{k-1} \rightarrow x_k) p(x_{k-1}, \vartheta_{k-1} | y_{1:k-1}) dx_{k-1} d\vartheta_{k-1} \quad (25)$$

$$p(x_k, \vartheta_k | y_{1:k}) \propto p(y_k | x_k; \mathrm{map}) p(x_k, \vartheta_k | y_{1:k-1}), \quad (26)$$

where $M(x_{k-1} \rightarrow x_k)$ represents map constraints.

The term $p(\boldsymbol{y}_k|\mathbf{x}_k; \text{map})$ in (26) denotes the localization result of UWB SAL system. As for pedestrian localization, the z-coordinate of localization results makes little sense. Therefore, 3D SPIs in local coordinate system (LCS) calculated by Algorithm 1 are first transformed into WCS and then converted into 2D coordinates. In addition, two penalty terms are added to the covariance matrix. On one hand, when a localization result is far away from the plane where the pedestrian is, it is probably an erroneous measurement and a penalty term $\boldsymbol{\Sigma}_{\text{h}}$ is added. On the other hand, NLOS propagation can be detected using map information, and a penalty term $\boldsymbol{\Sigma}_{\text{NLOS}}$ is added for reducing the impact of non-ideal measurements on localization results.[3] Finally, the observation likelihood is given by

$$p(\boldsymbol{y}_k|\boldsymbol{x}_k; \text{map}) = \sum_{l=1}^{L_k} \beta_k^l \mathcal{N}(\boldsymbol{x}_k; \hat{\boldsymbol{p}}_{\text{ML},k}^l, \boldsymbol{\Sigma}_k^l), \qquad (27)$$

and

$$\hat{\boldsymbol{p}}_{\text{ML},k}^l = \boldsymbol{\Gamma}(\boldsymbol{R}_a \hat{\boldsymbol{p}}_{\text{ML,LCS}}^l + \boldsymbol{p}_a)$$
$$\boldsymbol{\Sigma}_k^l = \boldsymbol{\Gamma} \boldsymbol{R}_a \boldsymbol{\Sigma}_{\text{LCS}}^l \boldsymbol{R}_a^{\text{T}} \boldsymbol{\Gamma}^{\text{T}} + \boldsymbol{\Sigma}_{\text{h}} + \boldsymbol{\Sigma}_{\text{NLOS}},$$

where $\boldsymbol{R}_a$ is the rotation matrix converting from LCS into WCS, $\boldsymbol{p}_a$ is the coordinate of LCS origin in the WCS, and $\boldsymbol{\Gamma}$ converts 3D coordinates into 2D coordinates.

Due to the non-linearity and non-Gaussianity of system model, PDF of state variables cannot be described in analytical expressions. By discretizing floor plan, we approximate the PDF by weights on discrete grid points.

1) Grid-based Filters on Coarse Grids: By discretization, we discretize the state space of location into N_{p} uniform grids $\{\boldsymbol{x}^{(i_{\text{p}})}\}_{i_{\text{p}}=1}^{N_{\text{p}}}$ and the state space of heading direction into N_{h} uniform angles $\{\vartheta^{(i_{\text{h}})}\}_{i_{\text{h}}=1}^{N_{\text{h}}}$. Then, the PDF of state variable is approximated by

$$p(\boldsymbol{x}_k, \vartheta_k|\boldsymbol{y}_{1:k}) \approx \sum_{(i_{\text{p}}, i_{\text{h}})} w_{k|k}^{(i_{\text{p}}, i_{\text{h}})} \delta(\boldsymbol{x}_k - \boldsymbol{x}^{(i_{\text{p}})}) \delta(\vartheta_k - \vartheta^{(i_{\text{h}})}), \qquad (28)$$

where $\delta(\cdot)$ is the delta function and $w_{k|k}^{(i_{\text{p}}, i_{\text{h}})}$ is the posterior weight at location $\boldsymbol{x}^{(i_{\text{p}})}$ and heading $\vartheta^{(i_{\text{h}})}$. After normalizing the weights such that they sum up to one, the estimated position is calculated by $\hat{\boldsymbol{x}}_{k|k} = \sum_{(i_{\text{p}}, i_{\text{h}})} w_{k|k}^{(i_{\text{p}}, i_{\text{h}})} \boldsymbol{x}^{(i_{\text{p}})}$.

Then, by substituting (28) into (25) and (26), we obtain

$$w_{k|k-1}^{(i_{\text{p}}, i_{\text{h}})} = \sum_{(j_{\text{p}}, j_{\text{h}})} w_{k-1|k-1}^{(j_{\text{p}}, j_{\text{h}})} M(\boldsymbol{x}^{(j_{\text{p}})} \to \boldsymbol{x}^{(i_{\text{p}})})$$
$$\cdot p(\boldsymbol{x}_k^{(i_{\text{p}})}, \vartheta_k^{(i_{\text{h}})}|\boldsymbol{x}_{k-1}^{(j_{\text{p}})}, \vartheta_{k-1}^{(j_{\text{h}})}, \boldsymbol{m}_k) \qquad (29)$$
$$w_{k|k}^{(i_{\text{p}}, i_{\text{h}})} \propto w_{k|k-1}^{(i_{\text{p}}, i_{\text{h}})} p(\boldsymbol{y}_k|\boldsymbol{x}_k^{(i_{\text{p}})}, \vartheta_k^{(i_{\text{h}})}; \text{map}). \qquad (30)$$

According to Bayes' theorem, the transition probability in (29) can be further written into

---

3. The value of penalty term is chosen empirically to be $(0.8\text{m})^2 \boldsymbol{I}_{2\times2}$ according to measurement results under NLOS conditions in [55].

$$p(\boldsymbol{x}_k^{(i_{\text{p}})}, \vartheta_k^{(i_{\text{h}})}|\boldsymbol{x}_{k-1}^{(j_{\text{p}})}, \vartheta_{k-1}^{(j_{\text{h}})}, \boldsymbol{m}_k) \propto p(\boldsymbol{x}_k^{(i_{\text{p}})}|\boldsymbol{x}_{k-1}^{(j_{\text{p}})}, \vartheta_{k-1}^{(j_{\text{h}})}, \boldsymbol{m}_k)$$
$$\cdot p(\vartheta_k^{(i_{\text{h}})}|\vartheta_{k-1}^{(j_{\text{h}})}, \Delta\vartheta_k), \qquad (31)$$

where the two terms are transitions of location probability and heading direction probability respectively. Since UWB measurements are independent with the heading direction in UWB observation likelihood described in (27), the heading direction $\vartheta_k^{(i_{\text{h}})}$ in (30) can be omitted. When there is no valid UWB measurements at some time instant, the update stage is omitted simply.

2) Fine-Grained Transition Grids: The accuracy of approximating arbitrary distributions by weights on grid points is highly related to discretization granularity. Decreasing quantization interval to achieve higher accuracy will cause the square increase of computational and memory complexity, which is not efficient. Because the expectation of location probability is more important in localization problem, a method calculating the transition probability on fine-grained grids is proposed, which keeps the expectation almost the same as the continuous PDF.

Fine-grained transition grids $\{\tilde{\boldsymbol{x}}^{(i_{\text{f}})}\}_{i_{\text{f}}=1}^{N_{\text{f}}}$ are introduced to capture the uncertainty of stride length $\text{SL}_k \sim \mathcal{U}(\widehat{SL}_k - \Delta SL, \widehat{SL}_k + \Delta SL)$ and heading direction $\theta_k \sim \mathcal{N}(\vartheta_{k-1}^{(j_{\text{h}})} + \Delta\vartheta_k, \sigma_\vartheta^2)$. Coordinates of fine-grained transition grids are determined by uniformly discretizing stride length and heading direction and the probability is calculated by

$$p(\tilde{\boldsymbol{x}}^{(i_{\text{f}})}|\vartheta_{k-1}^{(j_{\text{h}})}, \boldsymbol{m}_k) \propto p_{\text{SL}_k}(||\tilde{\boldsymbol{x}}^{(i_{\text{f}})}||) p_{\theta_k}(\mathcal{A}(\boldsymbol{0}, \tilde{\boldsymbol{x}}^{(i_{\text{f}})})),$$

where $\mathcal{A}(\boldsymbol{0}, \tilde{\boldsymbol{x}}^{(i_{\text{f}})})$ is the angle from $\boldsymbol{0}$ to $\tilde{\boldsymbol{x}}^{(i_{\text{f}})}$. The probability of fine-grained transition grid $\tilde{\boldsymbol{x}}^{(i_{\text{f}})}$ is distributed to adjacent coarse grid $\boldsymbol{x}^{(i_{\text{p}})} = (x^{(i_{\text{p}})}, y^{(i_{\text{p}})})$ multiplied by

$$c(\tilde{\boldsymbol{x}}^{(i_{\text{f}})}, \boldsymbol{x}^{(i_{\text{p}})}) = \frac{\Delta - |\tilde{x}^{(i_{\text{f}})} - x^{(i_{\text{p}})}|}{\Delta} \frac{\Delta - |\tilde{y}^{(i_{\text{f}})} - y^{(i_{\text{p}})}|}{\Delta}, \qquad (32)$$

where Δ is the quantization interval. The location transition probability in (31) is approximated by

$$p(\boldsymbol{x}_k^{(i_{\text{p}})}|\boldsymbol{x}_{k-1}^{(j_{\text{p}})}, \vartheta_{k-1}^{(j_{\text{h}})}, \boldsymbol{m}_k)$$
$$\approx \sum_{i_{\text{f}}=1}^{N_{\text{f}}} c(\boldsymbol{x}_{k-1}^{(j_{\text{p}})} + \tilde{\boldsymbol{x}}^{(i_{\text{f}})}, \boldsymbol{x}_k^{(i_{\text{p}})}) p(\tilde{\boldsymbol{x}}^{(i_{\text{f}})}|\vartheta_{k-1}^{(j_{\text{h}})}, \boldsymbol{m}_k). \qquad (33)$$

Proposition 2. *If the transition probability is calculated by (32) and (33), then the transition probability is only related to the relative location of coarse grid points and the mean value of the coarse grids is equal to that of the fine-grained grids, i.e.,*

(i) $\quad p(\boldsymbol{x}_k^{(i_{\text{p}})}|\boldsymbol{x}_{k-1}^{(j_{\text{p}})}, \vartheta_{k-1}^{(j_{\text{h}})}, \boldsymbol{m}_k) = p(\boldsymbol{x}_k^{(i_{\text{p}})} - \boldsymbol{x}_{k-1}^{(j_{\text{p}})}|\boldsymbol{0}, \vartheta_{k-1}^{(j_{\text{h}})}, \boldsymbol{m}_k)$

(ii) $\quad \mathbb{E}\left\{p(\boldsymbol{x}_k^{(i_{\text{p}})}|\boldsymbol{x}_{k-1}^{(j_{\text{p}})}, \vartheta_{k-1}^{(j_{\text{h}})}, \boldsymbol{m}_k)\right\}$
$$= \mathbb{E}\left\{p(\tilde{\boldsymbol{x}}^{(i_{\text{f}})}|\vartheta_{k-1}^{(j_{\text{h}})}, \boldsymbol{m}_k)\right\} + \boldsymbol{x}_{k-1}^{(j_{\text{p}})}.$$

Proof. See Appendix A, which can be found on the Computer Society Digital Library at http://doi.ieeecomputersociety.org/10.1109/TMC.2021.3083613. □
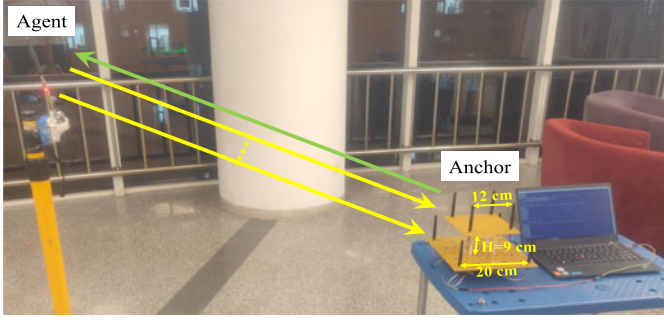
Fig. 4. An illustration of the proposed system. The anchor is placed at a stable place, and the agent is fixed on a tripod or held in hands. The anchor consists of two groups of four antennas with different heights.

Remark 3. Proposition 2 shows that the fine-grained transition grids can reduce computational and memory complexity significantly. Result (i) enables us to compute (33) once for each possible heading direction $\theta_{k-1}^{(j_h)}$. Result (ii) shows that the mean value of the coarse grids is the same as that of the fine-grained grids regardless of quantization interval, which enables increasing quantization interval without loss of accuracy.

During filtering, only those grids with high probabilities are kept in memory for the consideration of computational and memory complexity. After each prediction step and update step, the weights are normalized such that the maximum is one and those weights less than a threshold are removed. The expectation of those coarse grids with weight larger than a threshold is the estimated location. The overall algorithm is summarized in Algorithm 3.

6 EVALUATIONS

In this section, we evaluate the localization accuracy of the parallel SPI estimation algorithm and the tracking performance of GSKF and multi-grain grid-based filter. We first introduce the experiment setup, and then present simulation results of Algorithm 1 and experimental results in different scenarios. Finally, contributions of different measurements and algorithms to localization accuracy and ambiguity resolution are analyzed. Experimental results show that the proposed system can achieve decimeter-level localization.

6.1 Experiment Setup & Metrics

Our system consists of a hardware part and a software part. The hardware part includes a single-antenna agent and an eight-antenna anchor. Each antenna is connected to a Deca-Wave DW1000 UWB transceiver, which is capable of extracting ToA and carrier phase. All UWB transceivers are driven by a same clock reference. However, due to imperfection of clock circuits and channel noise, a calibration process is required and TDoA measurements can be refined in a real system, which are described in Appendix B, available in the online supplemental material.

All antennas form two squares with different heights. The bottom square has one side of 20 cm and is in XY plane, while the upper square has one side of 12 cm and is in the plane with $z = 9$ cm, as shown in Fig. 4. The centers of two squares are on the Z-axis. In the experiments, carrier

frequency of 4 GHz is used, the wavelength of which is about 6.7 cm. In each time slot, agent transmits multiple response messages (≥ 2) after receiving an initial message transmitted by the master antenna of anchor. The anchor receives messages and extracts raw measurements including distance, TDoA, and PDoA measurements. A typical usage scenario is illustrated in Fig. 4.

We implement Algorithm 1 with NVIDIA CUDA Toolkit 10.2 which can accelerate computing with GPU. All other algorithms are implemented using Java and run on a computer with Intel i7-4790k CPU. It is worth mentioning that the localization system is able to track agents in real time. The computing power of Nvidia GTX960 GPU is capable of executing Algorithm 1 three thousand times per second, which is much faster than the data sampling rate of UWB array 50 Hz. Algorithm 3 can run on a Google Nexus 6p smartphone in real time, which is validated in [10]. In addition, an Android application is developed to collect readings of IMU embedded in smartphones.

To evaluate the localization performance of the proposed system, we conduct experiments in outdoor open space and indoor environment. The outdoor open space is a square area with a $16 \text{ m} \times 16 \text{ m}$ area. There are some reflective objects and scattering objects in the outdoor environment including ground, buildings, and walking people, which affect the localization system negatively. Both static experiments and dynamic experiments using GSKF without IMU are conducted outdoors. The indoor environment is a typical office environment with a $16 \text{ m} \times 9 \text{ m}$ rectangular area, the floor plan of which is shown in Fig. 9a. Only dynamic experiments using Algorithm 3 are conducted. The performance metrics are listed below:

- Root mean squared error (RMSE): We measure the localization error by euclidean distance between estimated location and ground truth. The RMSE is chosen as the performance metric and those ambiguous position estimations are excluded. In dynamic experiments, we marked turning points of test trajectories and asked volunteers to walk in a straight line between those marked points. Distances between localization results and the preset trajectory are taken as localization errors.

- Success rate of ambiguity resolution (SR-I): If we take the most weighted output as the positioning result, SR-I measures the ratio of correct results.

- Success rate with filtering (SR-II): Algorithm 1 will calculate several ambiguous positions with larger weights. Due to measurement noises, the most weighted output is not necessarily the correct position. However, position ambiguities can be resolved by information fusion if the multiple outputs contain the correct position, the ratio of which is denoted as SR-II.

- Degree of ambiguity (DA): We take the ratio of the weight sum of wrong Gaussian components given by Algorithm 1 to the total number of measurements as DA, which reflects the ambiguity of an array geometry to a certain extent. Larger DA represents more ambiguities, which means more difficult to resolve ambiguities.
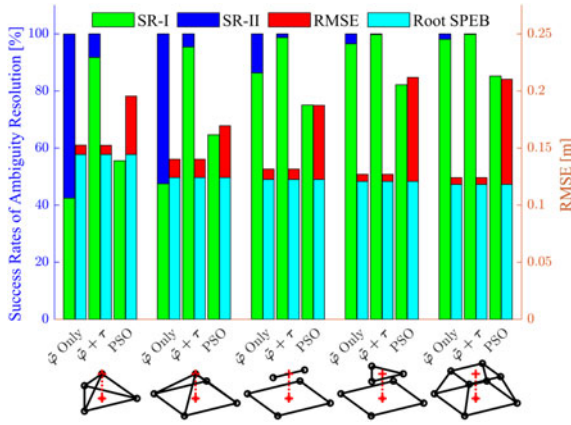
Fig. 5. Simulation results of different array geometries with similar aperture and comparison with particle swarm optimization (PSO) algorithm.
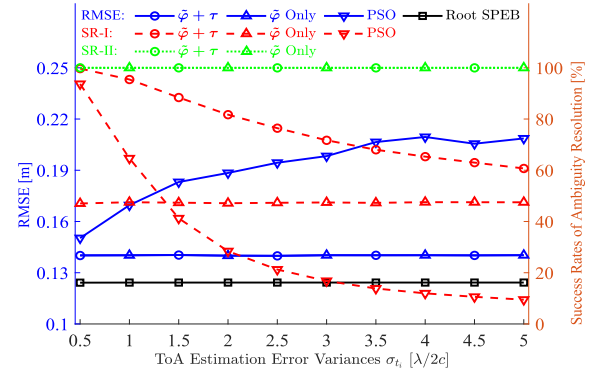

Fig. 6. Simulation results of localization accuracy and success rate of ambiguity resolution as the noise in ToA estimation increases using the anchor with 5 antennas.

TABLE 1
Degree of Ambiguity of Different Array Geometries

Antenna Number	4	5	6	7	8
$\tilde{\varphi}$ Only	69.4%	65.8%	19.1%	5.06%	2.67%
$\tilde{\varphi} + \tau$	14.1%	7.65%	2.18%	0.39%	0.28%

6.2 Simulation Results

We validate the effectiveness and efficiency of the proposed parallel SPI estimation algorithm through numerical simulations. We randomly choose 100,000 test points on the upper hemisphere with a radius of 10 m. Distance measurement, ToAs and PoAs are calculated according to (1), (2) and (3) respectively. In all simulations, carrier frequency of 4 GHz is used, the wavelength of which is about 6.7 cm. Distance measurement noise is set to be 0.1 m and PoA measurement noise is set to be $5°$. ToA measurement noise is set to be $\lambda/2c$ in the simulations of Fig. 5 and varies between 0.5 to 5 times of $\lambda/2c$ in the simulations of Fig. 6. The performance of the proposed method is compared to that of particle swarm optimization (PSO) algorithm optimizing the same log-likelihood function as (8). According to [29], 20 swarms are used to calculate the initial position with distance and TDoA measurements. Then, 1,000 swarms are used to global final optimal position with all measurements.

First, we study the impact of different array topologies on the performance of the proposed algorithm. Five different array geometries with similar aperture are simulated, the antenna number of which varies from 4 to 8. All antennas are distributed into two planes with heights of 0 cm and 9 cm. The spacings between adjacent antennas on the bottom and upper planes are 20 cm and 12 cm, respectively. Simulation results are shown in Fig. 5 and Table 1.

We evaluate the performance of Algorithm 1 using all measurements ($\tilde{\varphi} + \tau$) and not using TDoA measurements ($\tilde{\varphi}$ Only). The result shows that TDoA measurements can improve SR-I (green bar) and reduce DA (Table 1) of antenna array, but cannot improve the localization accuracy. It is worth mentioning that regardless of whether there is TDoA measurement, SR-II (blue bar) is close to 100 percent, demonstrating the stability of the proposed algorithm. The RMSE (red bar) can reach the lower bound (cyan bar), indicating

the high accuracy of Algorithm 1. Since PSO algorithm has only one output, SR-I is equal to SR-II. The simulation result shows that PSO algorithm cannot always find the global minimum because of large initial positioning error.

In the second simulation, we test the impact of different ToA measurement accuracies and the array with 5 antennas is used. As ToA noise gets larger, RMSE (blue line) and SR-II (green line) of the proposed algorithm remain nearly unchanged. However, SR-I (red line) gets worse because ToA measurement noise affects the calculation of Gaussian component weights as shown in Fig. 2. As a comparison, the performance of PSO algorithm deteriorates rapidly.

We also record the average computational time of the proposed algorithm and PSO algorithm. The proposed algorithm costs 229 us and 261 us per calculation in average of the case without and with TDoA measurements on the computer respectively. However, PSO algorithm implemented with MATLAB optimization toolbox costs about 3.9 s per calculation using one CPU core running at 2.3 GHz, which demonstrates the efficiency of our algorithm.

6.3 Experimental Results

We conduct outdoor static experiment, outdoor walking experiment, and indoor walking experiment. In static experiment, 88 test points are selected to evaluate the fixed-point localization performance of Algorithm 1. In dynamic experimental scenario, we select two outdoor trajectories and one indoor trajectory to evaluate the tracking performance of two filtering algorithms.

6.3.1 Outdoor Static Experiment

We first evaluate the performance of Algorithm 1 under static scenarios. We select a test point every 2 meters in the horizontal plane, a total of 44 test points. To validate the 3D positioning capability of the proposed SAL system, two planes with different heights are selected, one is 0.35 m and the other is 0.8 m, as shown by black crosses in Fig. 7a. The index of test points are assigned according to the distance to the origin. Each test point has 1,000 measurements, and localization results without filtering are represented by blue dots and red dots in Fig. 7a. Only correct Gaussian components are reserved in the plot. In addition, when collecting data at some test points such as 40L, some people walked

(a) Localization results   (b) RMSE and root SPEB at different distances   (c) CDF of localization error
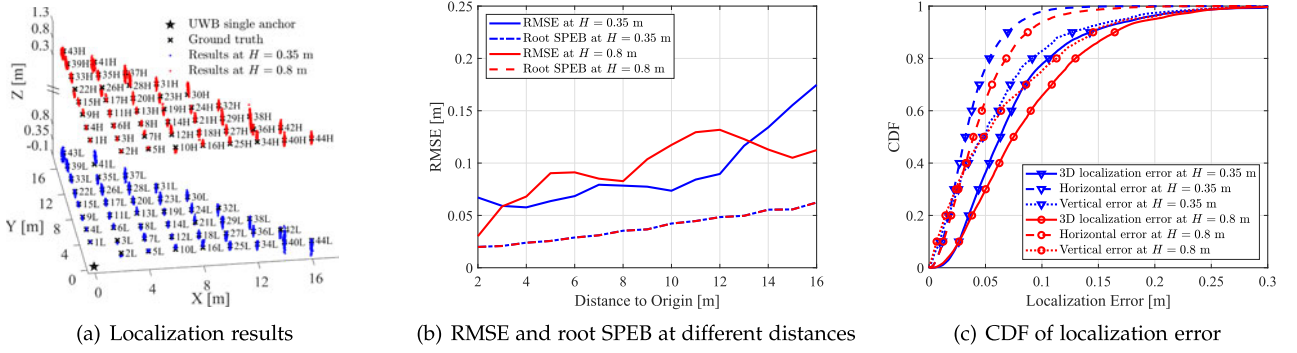
Fig. 7. Localization results in outdoor static experiment. (a) shows localization results of different test points (black cross) at $H = 0.35$ m (blue dots) and $H = 0.8$ m (red dots), and the anchor (black star) is placed at the origin. (b) shows the comparison of RMSE and root SPEB at different distances. (c) shows CDF curves of 3D localization error (solid lines), horizontal error (dashed lines), and vertical error (dotted lines).

through the LOS path between the anchor and the agent, which causes fluctuations in localization results. From another point of view, horizontal fluctuations are not very large, which shows the robustness of SAL system.

Comparison between RMSE of 3D localization results and SPEB of each test point is shown in Fig. 7b. At each distance, the RMSE is obtained by averaging the RMSE of nearby test points. Due to biases in TDoA and PDoA measurements, the positioning performance is difficult to reach the SPEB. At some test points with small measurement biases, the RMSE is very close to the SPEB. All measurements from 88 test points are used to construct the cumulative distribution function (CDF) of localization error. The RMSE of 3D localization results at all test points is 9.85 cm and the 90th percentile error is 15.6 cm. As shown in Fig. 7c, the RMSE of vertical localization is 8.4 cm which is worse than that of horizontal localization 5.15 cm, because the aperture in vertical direction of the array is relatively smaller than that in horizontal direction. In addition, the RMSE of localization results at a height of 0.35 m is 9.27 cm, which is 10 percent better than that at a height of 0.8 m. This is because the upper antenna support plate has a negative effect on the signal quality of bottom antennas and upper antennas are more likely to block LOS paths of lower antennas.

6.3.2 Outdoor Walking Experiment

To further evaluate the tracking performance of the proposed system using GSKF, a dynamic experiment is conducted outdoors. A person holds the agent and walks on an isosceles trapezoidal trajectory as shown by black solid lines in Fig. 8a. The trajectory starts at (10,0) m, passes through (0,10) m, (0,4) m, (4,0) m, and returns to the starting point. The person stands on the side of the agent away from the anchor to ensure that the LOS path between the agent and the anchor is not blocked. It should be noted that since the agent is handheld while walking, there will be errors in ground truth inevitably.

The blue and red solid lines in Fig. 8a are tracking results filtered by GSKF at different heights, and dots indicate origin localization results given by Algorithm 1 without filtering. The results show that the filtered localization results can follow the preset trajectory well. Since it is difficult to obtain the real-time ground truth, we take the distance between the localization result and the preset trajectory as the localization error, the CDF curves of which are shown in

Fig. 8b. The RMSE of 3D localization is 18.6 cm and the 90th percentile error is 29.5 cm.

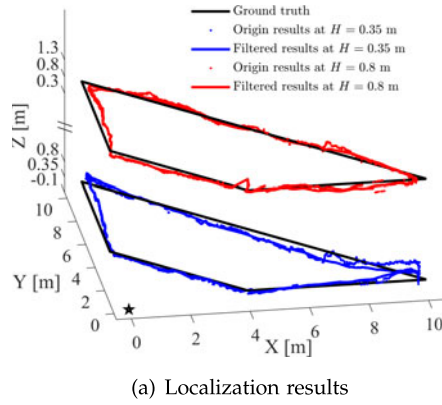### 6.3.3 Indoor Walking Experiment

We evaluate the performance of the proposed system in a typical office environment including two rooms, as shown in Fig. 9a. A person walks along the preset trajectory several times holding a smartphone to collect IMU readings and a UWB agent. The UWB anchor is placed at the center of one room marked as black star in Fig. 9a.

The blue line in Fig. 9a shows the estimated trajectory of an experiment by multi-grain grid-based filter, which is consistent with ground truth. The crosses are the localization results of UWB anchor. After obtaining UWB localization results, LOS or NLOS can be determined by utilizing floor plan. We mark localization results in LOS condition as green crosses, which are accurate. In NLOS conditions, there are positive errors in distance measurements and the stability of AoA estimation becomes worse, which are marked as red crosses. Localization results with low weight are marked as magenta crosses, which are possibly ambiguous results. In addition, localization results that have large height difference to the walking plane are removed.

The CDF of localization error is constructed using five repeated experiments and is shown in Fig. 9b. The RMSE is 24.5 cm and the 90th percentile error is 39.8 cm. We calculate the localization results of UWB anchor and filtering method in LOS and NLOS conditions separately. In LOS condition, the RMSE gets worse after filtering, because the localization error of UWB anchor is smaller than quantization interval. Approximating UWB localization results by weights on coarse grids will introduce quantization error. In practical application, we can use fusion results to resolve location ambiguities and take outputs of UWB anchor as final localization results in LOS condition. The NLOS propagation will introduce a positive error in distance measurement of UWB anchor and decrease the accuracy of AoA estimation. In this case, the multi-grain grid-based filter can decrease the RMSE of localization by 35 percent, from 45.4 cm to 29.5 cm.

6.4 Evaluation on Ambiguity Resolution and Accuracy

We measure the contributions of TDoA measurements and information fusion on resolving ambiguity and improving localization accuracy. In the case without TDoA
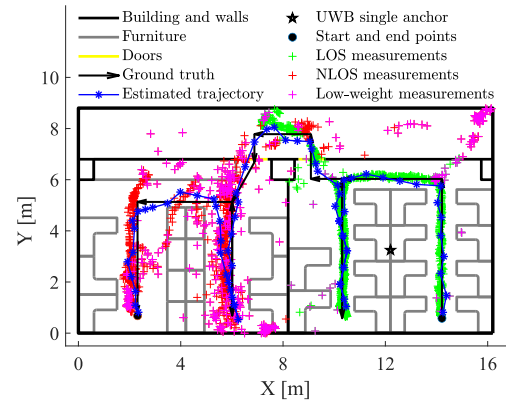
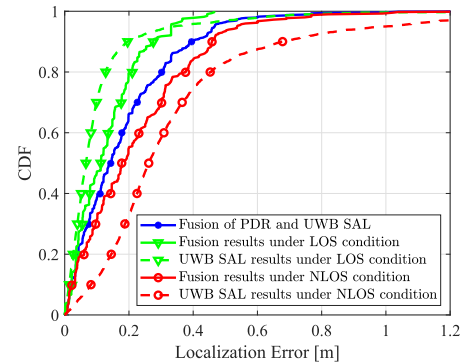(a) Localization results
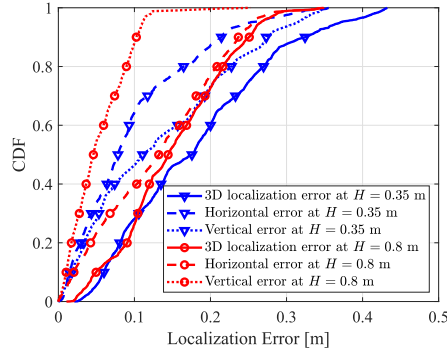
(b) CDF of localization error

Fig. 8. Localization results in outdoor walking experiment. (a) shows localization results before filtering (dots) and after filtering (solid lines) at $H = 0.35$ m (blue) and $H = 0.8$ m (red). (b) shows CDF curves of 3D localization error (solid lines), horizontal error (dashed lines), and vertical error (dotted lines) at different heights.

measurements, $\ell_\tau(\boldsymbol{p})$ is excluded from $\ell(\boldsymbol{p})$, the result of which is shown in the second column of Table 2. The results with TDoA measurements given by Algorithm 1 are listed in the third column. The results in the fourth column are filtered results by GSKF for outdoor scenario and multi-grain grid-based filter for indoor scenario.

By comparing results in the second column and the third column, we find that using TDoA measurements can significantly reduce degree of ambiguity, but is of little help in improving localization accuracy. In the outdoor static experiment, the ratio of ambiguous locations is low even without TDoA measurements because of the good signal quality. This shows that in LOS conditions, the antenna spacing can be further expanded or a higher carrier frequency can be used to improve localization accuracy. In such case, location ambiguities can almost be resolved by incorporating TDoA

(a) Localization results

(b) CDF of localization error

Fig. 9. Localization results in indoor walking experiment. (a) shows filtered localization results (blue line) by multi-grained grid-based filtering algorithm. Localization results of UWB SAL system are marked as crosses, including LOS (green), NLOS (red), and low-weight (magenta) measurements. (b) shows CDF curves of localization error before filtering (dashed lines) and after filtering (solid lines) under LOS (green) and NLOS (red) conditions.

measurements. However, when the agent is far away from the anchor or in a complex indoor environment (fourth row), the ratio of ambiguous locations increases due to the low signal quality. TDoA measurements can also resolve part of location ambiguities in such cases. NLOS propagations in indoor environments lead to wrong localization results, which makes the ratio of ambiguous locations high even with TDoA measurements.

The location ambiguities can be resolved accurately by filtering, as shown in the fourth column of Table 2. When there are ambiguities at the initial position, filters require several measurements to distinguish ambiguities, which causes the DA to be non-zero. In outdoor experimental

TABLE 2
Contributions of Different Modules to RMSE and Ambiguity Resolution

Experiments	PDoA		TDoA		Filtering	
	DA	RMSE	DA	RMSE	DA	RMSE
Simulation	32.4%	13.5 cm	4.91%	13.5 cm	_[a]	_[a]
Outdoor Static	1.83%	9.90 cm	$< 0.1\%$	9.85 cm	$< 0.1\%$	8.22 cm[b]
Outdoor Walking	4.61%	19.5 cm	$< 0.1\%$	19.4 cm	$< 0.1\%$	18.6 cm[b]
Indoor Walking	24.44%	18.8 cm	21.7%	18.7 cm	$< 0.1\%$	24.5 cm[c]

[a]*Since there is no temporal relationship between randomly generated test points, filtering is not applicable.*
[b]*GSKF without IMU measurements.*
[c]*Multi-grain grid-based filter.*

scenarios, filtering can slightly improve localization accuracy. However, the localization accuracy appears to get worse in indoor experiments after filtering, because many wrong UWB localization results with large errors are excluded from the RMSE under NLOS propagation conditions.

7 CONCLUSION

In this paper, we design a 3D SAL system based on antenna array with arbitrary geometry, which locates the agent using time and wrapped phase measurements of UWB signals. To improve localization accuracy, the antenna spacings are expanded to be larger than half-wavelength, and we address the angular ambiguity problem by information fusion. First, an efficient parallel SPI estimation algorithm is proposed to obtain parameters in SPI approximated by GMM, which can incorporate TDoA measurements optionally. Then, we propose GSKF and multi-grain grid-based filter to resolve location ambiguities in outdoor and indoor scenarios, respectively. The GSKF keeps track of location ambiguities and differentiate the real path as the measurement accumulates. The multi-grain grid-based filter fuses information from floor plan efficiently by calculating the transition probability on fine-grained grids and keeping weights on coarse grids. Experimental results show that location ambiguities can be resolved accurately and a 3D localization accuracy of 8.22 cm is achieved.

ACKNOWLEDGMENTS

REFERENCES

[1] M. Z. Win, Y. Shen, and W. Dai, "A theoretical foundation of network localization and navigation," *Proc. IEEE*, vol. 106, no. 7, pp. 1136–1165, Jul. 2018.

[2] W. Dai, Y. Shen, and M. Z. Win, "Energy-efficient network navigation algorithms," *IEEE J. Sel. Areas Commun.*, vol. 33, no. 7, pp. 1418–1430, Jul. 2015.

[3] Z. Liu, W. Dai, and M. Z. Win, "Mercury: An infrastructure-free system for network localization and navigation," *IEEE Trans. Mobile Comput.*, vol. 17, no. 5, pp. 1119–1133, May 2018.

[4] X. Tian, Z. Song, B. Jiang, Y. Zhang, T. Yu, and X. Wang, "HiQuadLoc: A RSS fingerprinting based indoor localization system for quadrotors," *IEEE Trans. Mobile Comput.*, vol. 16, no. 9, pp. 2545–2559, Sep. 2017.

[5] Q. Guo, Y. Zhang, J. Lloret, B. Kantarci, and W. K. G. Seah, "A localization method avoiding flip ambiguities for micro-UAVs with bounded distance measurement errors," *IEEE Trans. Mobile Comput.*, vol. 18, no. 8, pp. 1718–1730, Aug. 2019.

[6] Y. Liu, Y. Wang, J. Wang, and Y. Shen, "Distributed 3D relative localization of UAVs," *IEEE Trans. Veh. Technol.*, vol. 69, no. 10, pp. 11 756–11 770, Oct. 2020.

[7] F. Zafari, A. Gkelias, and K. K. Leung, "A survey of indoor localization systems and technologies," *IEEE Commun. Surveys Tuts.*, vol. 21, no. 3, pp. 2568–2599, Third Quarter 2019.

[8] M. Z. Win *et al.*, "Network localization and navigation via cooperation," *IEEE Commun. Mag.*, vol. 49, no. 5, pp. 56–62, May 2011.

[9] M. Z. Win, W. Dai, Y. Shen, G. Chrisikos, and H. Vincent Poor, "Network operation strategies for efficient localization and navigation," *Proc. IEEE*, vol. 106, no. 7, pp. 1224–1254, Jul. 2018.

[10] F. Ge and Y. Shen, "Realtime indoor localization on smartphones by multi-grained grid-based filters," in *Proc. IEEE Global Commun. Conf.*, 2018, pp. 1–7.

[11] X. Tong, K. Liu, X. Tian, L. Fu, and X. Wang, "FineLoc: A fine-grained self-calibrating wireless indoor localization system," *IEEE Trans. Mobile Comput.*, vol. 18, no. 9, pp. 2077–2090, Sep. 2019.

[12] H. Liu, J. Yang, S. Sidhom, Y. Wang, Y. Chen, and F. Ye, "Accurate WiFi based localization for smartphones using peer assistance," *IEEE Trans. Mobile Comput.*, vol. 13, no. 10, pp. 2199–2214, Oct. 2014.

[13] S. S. Saab and Z. S. Nakad, "A standalone RFID indoor positioning system using passive tags," *IEEE Trans. Ind. Electron.*, vol. 58, no. 5, pp. 1961–1970, May 2011.

[14] M. Kotaru, K. Joshi, D. Bharadia, and S. Katti, "SpotFi: Decimeter level localization using WiFi," in *Proc. ACM Conf. Special Interest Group Data Commun.*, 2015, pp. 269–282.

[15] Bluetooth SIG., *Bluetooth Core Specification 5.1* Kirkland, WA, USA, 2019. [Online]. Available: https://www.bluetooth.com/specifications/bluetooth-core-specification/

[16] M. Z. Win and R. A. Scholtz, "Impulse radio: How it works," *IEEE Commun. Lett.*, vol. 2, no. 2, pp. 36–38, Feb. 1998.

[17] M. Z. Win and R. A. Scholtz, "Ultra-wide bandwidth time-hopping spread-spectrum impulse radio for wireless multiple-access communications," *IEEE Trans. Commun.*, vol. 48, no. 4, pp. 679–691, Apr. 2000.

[18] D. Dardari, A. Conti, U. Ferner, A. Giorgetti, and M. Z. Win, "Ranging With ultrawide bandwidth signals in multipath environments," *Proc. IEEE*, vol. 97, no. 2, pp. 404–426, Feb. 2009.

[19] B. Großwindhager *et al.*, "SALMA: UWB-based single-anchor localization system using multipath assistance," in *Proc. ACM Conf. Sensys.*, 2018, pp. 132–144.

[20] H. Mohammadmoradi, M. Heydariaan, O. Gnawali, and K. Kim, "UWB-based single-anchor indoor localization using reflected multipath components," in *Proc. Int. Conf. Comput., Netw. Commun.*, 2019, pp. 308–312.

[21] Y. Liu, Y. Shen, and M. Z. Win, "Single-anchor localization and synchronization of full-duplex agents," *IEEE Trans. Commun.*, vol. 67, no. 3, pp. 2355–2367, Mar. 2019.

[22] L. Taponecco, A. A. D'Amico, and U. Mengali, "Joint TOA and AOA estimation for UWB localization applications," *IEEE Trans. Wireless Commun.*, vol. 10, no. 7, pp. 2207–2217, Jul. 2011.

[23] T. Wang, H. Zhao, and Y. Shen, "An efficient single-anchor localization method using ultra-wide bandwidth systems," *Appl. Sci.*, vol. 10, no. 1, Aug. 2020, Art. no. 57.

[24] I. Dotlic, A. Connell, H. Ma, J. Clancy, and M. McLaughlin, "Angle of arrival estimation using DecaWave DW1000 integrated circuits," in *Proc. Workshop Positioning, Navigation Commun.*, 2017, pp. 1–6.

[25] B. Friedlander and A. J. Weiss, "Direction finding in the presence of mutual coupling," *IEEE Trans. Antennas Propag.*, vol. 39, no. 3, pp. 273–284, Mar. 1991.

[26] Y. Shen and M. Z. Win, "On the accuracy of localization systems using wideband antenna arrays," *IEEE Trans. Commun.*, vol. 58, no. 1, pp. 270–280, Jan. 2010.

[27] T. Ballal and C. J. Bleakley, "Phase-difference ambiguity resolution for a single-frequency signal in the near-field using a receiver triplet," *IEEE Trans. Signal Process.*, vol. 58, no. 11, pp. 5920–5926, Nov. 2010.

[28] M. Wax and R. Tweg, "Direction of arrival tracking below the ambiguity threshold," *IEEE Trans. Aerosp. Electron. Syst.*, vol. 36, no. 2, pp. 354–363, Apr. 2000.

[29] H. Chen, T. Ballal, N. Saeed, M. S. Alouini, and T. Y. Al-Naffouri, "A joint TDOA-PDOA localization approach using particle swarm optimization," *IEEE Wireless Commun. Lett.*, vol. 9, no. 8, pp. 1240–1244, Aug. 2020.

[30] A. Conti, S. Mazuelas, S. Bartoletti, W. C. Lindsey, and M. Z. Win, "Soft information for localization-of-things," *Proc. IEEE*, vol. 107, no. 11, pp. 2240–2264, Nov. 2019.

[31] P. Meissner and K. Witrisal, "Multipath-assisted single-anchor indoor localization in an office environment," in *Proc. Int. Conf. Syst., Signals Image Process.*, 2012, pp. 22–25.

[32] J. Kulmer *et al.*, "Using DecaWave UWB transceivers for high-accuracy multipath-assisted indoor positioning," in *Proc. IEEE Int. Conf. Commun. Workshops*, 2017, pp. 1239–1245.

[33] F. Yao, Y. Wang, and X. Guan, "Joint time synchronization and localization for target sensors using a single mobile anchor with position uncertainties," in *Proc. IEEE Int. Conf. Acoust., Speech Signal Process.*, 2018, pp. 3794–3798.

[34] T. Lei, S. Pan, K. Wang, and Y. Yu, "Continuous TOA measurement based single-anchor indoor localization," *IEEE Access*, to be published, doi: 10.1109/ACCESS.2019.2941596.

[35] Z. Chen *et al.*, "M^3: Multipath assisted Wi-Fi localization with a single access point," *IEEE Trans. Mobile Comput.*, vol. 20, no. 2, pp. 588–602, Feb. 2021.

[36] M. Heydariaan, H. Dabirian, and O. Gnawali, "AnguLoc: Concurrent angle of arrival estimation for indoor localization with UWB radios," in *Proc. Int. Conf. Distrib. Comput. Sensor Syst.*, 2020, pp. 112–119.

[37] I. Ziskind and M. Wax, "Maximum likelihood localization of multiple sources by alternating projection," *IEEE Trans. Acoust., Speech, Signal Process.*, vol. 36, no. 10, pp. 1553–1560, Oct. 1988.

[38] J. Foutz, A. Spanias, and M. Banavar, *Narrowband Direction of Arrival Estimation for Antenna Arrays*. San Rafael, CA, USA: Morgan & Claypool, 2008.

[39] R. Schmidt, "Multiple emitter location and signal parameter estimation," *IEEE Trans. Antennas Propag.*, vol. 34, no. 3, pp. 276–280, Mar. 1986.

[40] R. Roy and T. Kailath, "ESPRIT-estimation of signal parameters via rotational invariance techniques," *IEEE Trans. Acoust., Speech, Signal Process.*, vol. 37, no. 7, pp. 984–995, Jul. 1989.

[41] A. Flieller, P. Larzabal, and H. Clergeot, "Study of ambiguities in array manifold: A general framework," in *Proc. Workshop Statist. Signal Array Process.*, 1996, pp. 574–577.

[42] A. Moffet, "Minimum-redundancy linear arrays," *IEEE Trans. Antennas Propag.*, vol. AP-16, no. 2, pp. 172–175, Mar. 1968.

[43] P. Pal and P. P. Vaidyanathan, "Nested arrays: A novel approach to array processing with enhanced degrees of freedom," *IEEE Trans. Signal Process.*, vol. 58, no. 8, pp. 4167–4181, Aug. 2010.

[44] P. P. Vaidyanathan and P. Pal, "Sparse sensing with co-prime samplers and arrays," *IEEE Trans. Signal Process.*, vol. 59, no. 2, pp. 573–586, Feb. 2011.

[45] M. D. Zoltowski and K. T. Wong, "ESPRIT-based 2-D direction finding with a sparse uniform array of electromagnetic vector sensors," *IEEE Trans. Signal Process.*, vol. 48, no. 8, pp. 2195–2204, Aug. 2000.

[46] Z. He, Z. Zhao, Z. Nie, P. Ma, and Q. H. Liu, "Resolving manifold ambiguities for sparse array using planar substrates," *IEEE Trans. Antennas Propag.*, vol. 60, no. 5, pp. 2558–2562, May 2012.

[47] M. Lin, P. Liu, and J. Liu, "DOA ambiguity suppressing by rotating the array," in *Proc. IEEE Asia-Pacific Conf. Antennas Propag.*, 2015, pp. 165–167.

[48] P. Hyberg, M. Jansson, and B. Ottersten, "Array interpolation and bias reduction," *IEEE Trans. Signal Process.*, vol. 52, no. 10, pp. 2711–2720, Oct. 2004.

[49] V. P. Ipatov, "Ternary sequences with ideal autocorrelation properties," *Radio Eng. Electron. Phys.*, vol. 24, pp. 75–79, Oct. 1979.

[50] D. Neirynck, E. Luk, and M. McLaughlin, "An alternative double-sided two-way ranging method," in *Proc. 13th Workshop Positioning, Navigation Commun.*, 2016, pp. 1–4.

[51] Y. Shen and M. Z. Win, "Fundamental limits of wideband localization – Part I: A general framework," *IEEE Trans. Inf. Theory*, vol. 56, no. 10, pp. 4956–4980, Oct. 2010.

[52] S. M. Kay, *Fundamentals of Statistical Signal Processing: Estimation Theory*. Upper Saddle River, NJ, USA: Prentice Hall, 1993.

[53] W. Zijlstra, "Assessment of spatio-temporal parameters during unconstrained walking," *Eur. J. Appl. Physiol.*, vol. 92, no. 1/2, pp. 39–44, Jun. 2004.

[54] V. Kubelka and M. Reinstein, "Complementary filtering approach to orientation estimation using inertial sensors only," in *Proc. IEEE Int. Conf. Robot. Autom.*, 2012, pp. 599–605.

[55] C. Mao, K. Lin, T. Yu, and Y. Shen, "A probabilistic learning approach to UWB ranging error mitigation," in *Proc. IEEE Global Commun. Conf.*, 2018, pp. 1–6.

Feng Ge (Student Member, IEEE) received the BE degree in electronic engineering from Tsinghua University, Beijing, China, in 2016. He is currently working toward the PhD degree in the Department of Electronic Engineering, Tsinghua University, China. His current research interests include indoor localization, cooperative localization, mobile sensor networks, and array signal processing.

Yuan Shen (Senior Member, IEEE) received the BE degree (with highest honor) in electronic engineering from Tsinghua University, Beijing, China, in 2005, and the SM and PhD degrees in electrical engineering and computer science from the Massachusetts Institute of Technology (MIT), Cambridge, Massachusetts, in 2008 and 2014, respectively. He is an associate professor with the Department of Electronic Engineering, Tsinghua University, China. His current research interest include network localization and navigation, resource allocation, inference techniques, and cooperative networks. He was the elected chair for IEEE ComSoc Radio Communications Committee for the period of 2019-2020. He has served as the TPC Symposium co-chair for the IEEE ICC and Globecom for several times. He is also an editor of the *IEEE Transactions on Wireless Communications*, *IEEE Wireless Communications Letters*, and *China Communications*.

▷ **For more information on this or any other computing topic, please visit our Digital Library at** www.computer.org/csdl.